Cross-Correlated TIRF/AFM Reveals Asymmetric Distribution of Force-Generating Heads along Self-Assembled, "Synthetic" Myosin Filaments

André E. X. Brown,[†‡] Alina Hategan,[§] Daniel Safer,[§] Yale E. Goldman,[‡§¶] and Dennis E. Discher[‡¶‖*]
[†]Department of Physics and Astronomy, [‡]Nano/Bio Interface Center, [§]Pennsylvania Muscle Institute, and Graduate Groups in [¶]Cell and Molecular Biology and [‖]Physics, University of Pennsylvania, Philadelphia, Pennsylvania 19104

ABSTRACT Myosin-II's rod-like tail drives filament assembly with a head arrangement that is often considered to be a symmetric bipole that generates equal and opposite contractile forces on actin. Self-assembled myosin filaments are shown here to be asymmetric in physiological buffer based on cross-correlated images from both atomic force microscopy and total internal reflection fluorescence. Quantitative cross-correlation of these orthogonal methods produces structural information unavailable to either method alone in showing that fluorescence intensity along the filament length is proportional to height. This implies that myosin heads form a shell around the filament axis, consistent with F-actin binding. A motor density of ~50–100 heads/micrometer is further estimated but with an average of 32% more motors on one half of any given filament compared to the other, regardless of length. A purely entropic pyramidal lattice model is developed and mapped onto the Dyck paths problem that qualitatively captures this lack of length dependence and the distribution of filament asymmetries. Such strongly asymmetric bipoles are likely to produce an unbalanced contractile force in cells and in actin-myosin gels and thereby contribute to motility as well as cytoskeletal tension.

INTRODUCTION

Myosin-II molecules are found in contractile ''bipolar'' filaments in cell types that range from striated muscle to stem cells (1). A number of these myosin-IIs are also known to self-assemble in vitro into active bipolar filaments, and both the structure and assembly characteristics of such ''synthetic'' filaments have been intensively studied for several decades—including recent work with atomic force microscopy (AFM) (2,3)—with most studies focusing on skeletal muscle myosin (4). Synthetic filaments have also found use in in vitro motility assays, where it has been shown that myosin arranged into ordered filaments moves actin filaments differently from single myosins randomly oriented on a surface (5–7). More recently, synthetic filaments have also been incorporated into cross-linked actin networks to make ''active gels'' that might be considered in vitro mimics of cellular cytoskeletal systems (8). Because of the long interest in using such filaments as model systems to study the motility and contractility of myosin, further insight into filament properties could be important.

Myosin filaments already have many well-characterized structural features and are therefore an excellent sample to develop ''cross-correlated TIRF/AFM'' in which two orthogonal imaging methods based, respectively, on optics and topography are mathematically compared and fit to a model. This provides the dual advantage of testing the reliability of the coupled method in a well-defined system while also opening up the possibility of new insights into these important motor filaments.

The model of thick filament structure first suggested by Huxley in 1963 (9) proposed that the 150-nm-long rod domain of myosin assembles in the core of the filament with the heads decorating the exterior of the filament; this model has stood the test of time. Many subsequent studies of myosin filament structure have focused on the mechanisms governing the filament length distribution, which, under certain conditions, can be quite close to the physiological length of 1.5 μm (10). The narrow length distribution is not the only feature that is important for muscle myosin filaments in vivo: they are found to be highly symmetric, which seems appropriate for muscle contraction (11). Although synthetic filaments have been shown to be bipolar in motility assays (6,7), their symmetry has not been sufficiently addressed before. In this article, we combine single-molecule fluorescence in TIRF microscopy with AFM tapping-mode imaging to study the arrangement of myosin heads in synthetic filaments, showing that their symmetry is not strictly controlled and fits a particularly random assembly model.

MATERIALS AND METHODS

Myosin purification and fluorescence labeling

Myosin was prepared from rabbit skeletal muscle as described by Margossian and Lowey (12). Myosin molecules were covalently labeled with tetramethylrhodamine-5-maleimide (Molecular Probes, Eugene, OR) or tetramethylrhodamine-5-iodoacetamide (AnaSpec, San Jose, CA) under conditions that favor labeling at Cys-707 in the myosin head (13) at ~1:1 stoichiometry. Myosin in 40 mM KCl, 5 mM sodium phosphate, 0.1 mM tris(2-carboxyethyl)phosphine, pH 7.0, was incubated at 4°C for 16 h with

Submitted June 10, 2008, and accepted for publication November 21, 2008.

*Correspondence: discher@seas.upenn.edu

André E. X. Brown and Alina Hategan contributed equally to this work.

Editor: Malcolm Irving.

0006-3495/09/03/1952/9 $2.00

doi: 10.1016/j.bpj.2008.11.032

either tetramethylrhodamine-5-maleimide or tetramethylrhodamine-5-iodoacetamide, at a ratio of 1:1. The labeled myosin was recovered by centrifugation at 12,000 × *g* for 10 min and was then redissolved in 0.6 M KCl, 10 mM imidazole-HCl, 2 mM $MgCl_2$, 1 mM dithiothreitol, pH 7.0, and dialyzed against the same buffer. The myosin stock had a concentration of 3.13 mg/mL and was stored in 50% glycerol solution at –20°C.

Myosin filament preparation

Myosin from the stock was diluted 10 times in 300 mM KCl, 5 mM $MgCl_2$, 10 mM Hepes buffer at pH 7, and centrifuged at 350,000 × *g* for 30 min at 4°C to sediment any aggregates, leaving single myosin molecules in the supernatant. Filament preparation was done by rapid mixing of myosin monomers in the supernatant solution with an equal volume of polymerization buffer (5 mM $MgCl_2$, 10 mM Hepes buffer at pH 7) or by dialysis in which the polymerization buffer was added in 15 steps at 1-min intervals during continuous mixing of the sample. Samples were incubated for 30 min at room temperature and then stored on ice. Experiments were performed on the same day the filaments were formed.

Sample preparation for TIRF/AFM

For AFM imaging, filaments from the polymerization vial were diluted 10 times in 150 mM KCl, 5 mM $MgCl_2$, 10 mM Hepes buffer at pH 7; 1 μL of 1 mg/mL BSA was added to 100 μL of this solution, and 50 μL of this solution was then allowed to adhere to clean glass slides that were spin-coated with poly(methyl methacrylate) (PMMA) (Sigma-Aldrich, Saint Louis, MO, catalog number: 370037) for 1 min. The sample was then gently washed with the same buffer used for dilution.

Hybrid TIRF/AFM

A Veeco Bioscope II AFM mounted on a Nikon TE 200 inverted optical microscope was equipped with an Olympus oil immersion TIRF objective (60× magnification, 1.45 numerical aperture). Fluorescence was excited using a 300-mW 532-nm laser (B&W TEK, Newark, DE) whose intensity was adjusted by rotating one of two crossed polarizers to minimize photobleaching while still allowing for single-molecule imaging with a reasonable frame rate. The beam was then directed into the back of the microscope from a mirror with an adjustable angle and converging lens used to control the position of the beam within the objective and therefore the angle of incidence at the sample coverslip. The incident angle was set to obtain strong reflection from the PMMA-water interface without cutting off the intensity at the objective back focal plane aperture. Using an AFM tip coated with fluorescent protein, we measured the spatial decay length of the evanescent field to be 140 nm (Appendix A), corresponding to an incident angle in the glass of 63°.

Fluorescence images were collected on a 16-bit Cascade 512B EMCCD camera (Photometrics, Tucson, AZ) with a frame interval of 50 ms. Each image was 512 by 512 pixels with no additional binning.

AFM imaging

All AFM imaging was done in buffer in tapping mode using either DNP-S or MSCT silicon nitride cantilevers (Veeco, Santa Barbara, CA). Images were 512 by 512 pixels large and were taken with a variety of tip velocities, usually around 10 μm/s. AFM images were taken at regions of interest determined from previously captured TIRF images based on the known tip location as determined from brightfield imaging of the cantilever.

Image analysis

Registration was done manually based on the known region of interest determined from the TIRF image before AFM imaging. Height and intensity profiles were measured along the center line of the filaments using NIH ImageJ after the filaments had been straightened using the Straighten plugin by Kocsis et al. (14). The profiles show the intensity at each point along the length without any averaging or interpolation between pixels. All other analysis was performed using Mathematica (Wolfram Research, Champagne, IL). The data for the height-intensity scaling plot (see Fig. 3 *a*) were taken from the filaments shown in Fig. 2 and two others from a different region that were long enough for profiles to be determined from the TIRF image and that were also well separated and in regions with low background fluorescence.

RESULTS AND DISCUSSION

AFM versus TIRF resolution

Single-molecule imaging by fluorescence has been achieved with a large number of systems, but always when individual fluorophores were separated by a distance greater than the diffraction limit (15) or were activated or bleached sequentially and thus effectively separated in time (16). In filaments, myosin molecules and therefore fluorophores are crowded into a tight space, well beyond the diffraction limit of a light microscope. Indeed, when formed by rapid mixing, filaments proved too short for any structural information to be determined from the TIRF images alone (Fig. 1 a), but the bright spots visible in TIRF clearly show the presence of spots that fluoresce too intensely to be single molecules (per intensity analyses below). However, when the same region is imaged with AFM, the pixillated spots are resolved into filaments with the clearly tapered ends expected for myosin filaments prepared under these conditions (Fig. 1 b) (17). Lengths can also be accurately determined as 0.9 ± 0.2 μm (mean ± SD), which is somewhat shorter than the physiological length of 1.5 μm (9).

Because of the significant resolution advantage offered by AFM, it might not be immediately clear that the two images do in fact show the same region of the sample. To aid in comparison, the TIRF image was thresholded, and the outline of this thresholded image is shown as the white overlay in Fig. 1 b. It should now be clear that both images show the same sample region and that the brightest regions in TIRF are in fact caused by several filaments that cannot be resolved optically. The AFM used has a closed-loop position sensor that corrects possible errors from piezo nonlinearity, hysteresis, and drift and allows specific regions to be imaged at still higher resolution in AFM to look for more detailed structural features of the samples than is possible in fluorescence (compare Fig. 1, *c* and *d*). At this resolution, the tapered structure becomes more apparent, and it is clear that there is no central bare zone—a region without myosin heads—as expected for pH 7 filaments (17).

Quantitative cross-correlation of TIRF and AFM data

Longer myosin filaments with a broader length distribution 3 ± 2 μm (mean ± SD) are formed when dialysis is used to slowly reduce the ionic strength of a solution of myosin

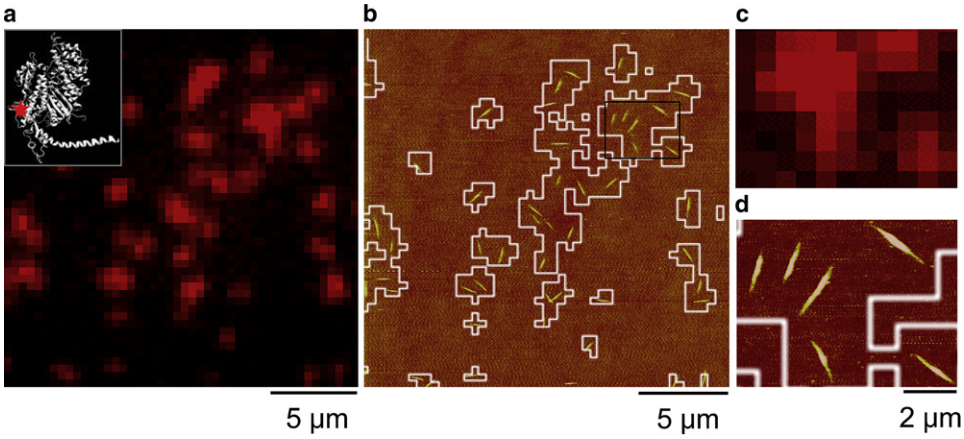

FIGURE 1 TIRF and AFM images of self-assembled myosin filaments on PMMA-coated glass in buffer with physiological salt. Myosin molecules were labeled with an average of 1.2 dyes per heavy chain and predominantly at Cys-707 in the motor domain. (*a*) The TIRF image has limited resolution both because of diffraction effects and because of the finite pixel size of the camera. The inset shows the crystal structure of the myosin motor domain with part of the converter domain. The red star indicates Cys-707. (*b*) Tapping mode AFM height image of the same region shows the elongated and tapered structure of individual myosin filaments that are now clearly resolved. The white overlay represents the edge of the thresholded TIRF image to demonstrate registration. (*c*) Cropped and scaled TIRF image from the region indicated with the black box in *b*. (*d*) Rescan of the same region by AFM reveals still higher resolution and finer structural details of the filaments.

monomers (Materials and Methods). Filaments formed using this method have proven useful for in vitro motility assays because actin movement can be tracked over longer distances that can be clearly observed in optical microscopy (6). In the case of combined TIRF/AFM, the fact that longer filaments can be clearly resolved in TIRF makes a quantitative comparison of fluorescence and height data possible. Fig. 2 *a* shows a TIRF image of three myosin filaments, and Fig. 2 *b* shows the AFM height image of the same region. The images are clearly similar, and quantitative analyses add further insight.

Intensity and height profiles taken along the filament centerlines are plotted in Fig. 2 *c* (fluorescence intensity in red and height in black). To facilitate comparisons by taking the broadening of the optical microscope into account, we smoothed the AFM height profiles by convolution with a Gaussian kernel with the same standard deviation as that determined from fits to the intensity profiles of single

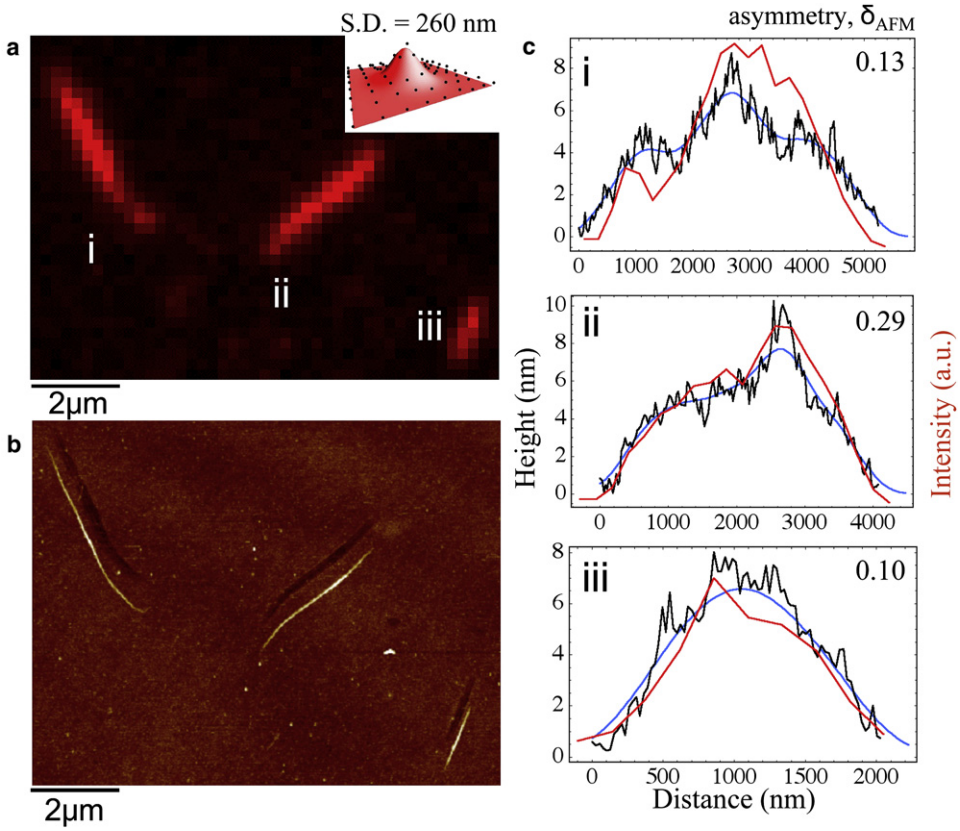

FIGURE 2 Fluorescence intensity (and therefore number of myosin heads) correlates with height. (*a*) TIRF image. Inset shows the optical microscope's point spread function (PSF) determined by fitting a Gaussian (standard deviation 260 nm) to a single spot in a TIRF image. (*b*) Tapping-mode AFM height image of the same region. The "shadows" vertically displaced above the filaments are most likely a tip artifact, but because they are several filament widths away from the principal image, this artifact is unlikely to affect the tip tracking and height profiles along the filament lengths. (*c*) Maximum height (*black*) and intensity (*red*) profiles measured along the three filaments in the images. The blue curve is the convolution of the AFM trace with the PSF to simulate broadening of fluorescence by diffraction and to facilitate a more appropriate comparison between height and intensity. The number in the top right of each plot is the fractional asymmetry of each filament calculated assuming the filaments have a circular cross section. It is an estimate of how much more volume the filament has on one half than on the other divided by the total volume.

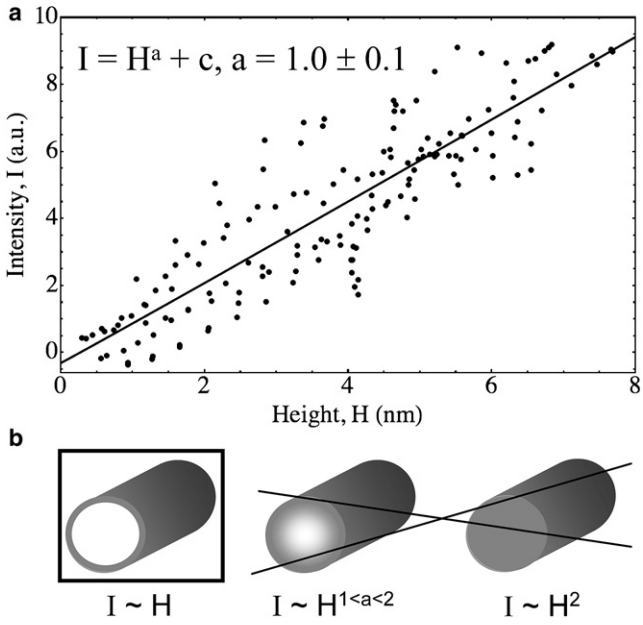

FIGURE 3 Height-intensity scaling and its structural implications. (*a*) Plot of intensity versus height calculated using the broadened AFM height data. The black curve is a power law fit with a resulting exponent of 1.0 ± 0.1, suggesting that the best scaling is linear; indeed, the Akaike information criterion shows that a linear fit is three times more likely to account for the data than the power law fit and 3×10^6 times more likely than a quadratic fit. Linear scaling implies that the myosin heads are arranged in a shell around the filament, if this were not the case, the number of dyes present in a given diffraction-limited cross section would scale as a higher power of the diameter (and therefore height) as illustrated schematically in (*b*).

fluorophores (Fig. 2 *a*, *inset*). The smoothed height profile is shown in blue.

The agreement between the two methods is clear on inspection, but to make these observations more precise, we made a height-intensity scatter plot using the profiles in Fig. 2 *c* as well as two from another sample region. The intensity is fit with a function of the form $I = H^a + c$ with $a = 1.0 \pm 0.1$, suggesting that the scaling is linear. To confirm that the data are in fact represented better by a linear model, we used the Akaike information criterion (18,19). This is useful because simply considering the goodness of fit will favor models with more parameters. In the extreme case of a polynomial with the same degree as the number of data points, the fit will always be perfect. In contrast, the Akaike information criterion balances this increase in goodness of fit with a term that depends on the number of parameters. The results of this analysis can be converted to evidence ratios (19) that revealed a linear fit is three times more likely to account for the data than a power law fit and is 3×10^6 times more likely than a quadratic fit. This linear scaling is not obvious a priori and, in fact, reveals information about filament structure that is not available from either TIRF or AFM alone. In particular, because height simply reflects the filament diameter, whereas intensity reflects the total number of fluorophores in a filament cross-section, linear scaling implies that the fluorophores, which reside in the myosin head, are arranged in a shell around the filament. In other words, if the heads are arranged in a shell around the filament, they will form a circle in cross section. If their diameter is doubled, the circumference of this circle and therefore the number of myosin heads will also double. In contrast, had the labeling been uniform throughout the filament, a quadratic scaling would be expected because in this case the intensity would scale as the filament cross-sectional area, whereas the height would still reflect the filament diameter. An intermediate scenario with some labeled heads in the filament interior might also have been possible, but this is three times less as likely to account for the observed data as determined by the Akaike information criterion. These possibilities are displayed schematically in Fig. 3 *b*.

The analyses above could be complicated by several factors. The first is that the evanescent field used to excite fluorescence in TIRF decays exponentially from the sample surface so that heads on the top of a filament will experience a smaller excitation intensity than those on the surface. However, this correction can be shown to be negligible based on reasonable assumptions about the parameters of this experiment and a direct measurement of the fluorescence intensity as a function of height (see Appendix A). Another potential source of error comes from inhomogeneities in the excitation across the field of view that distort the intensity along the filament length. Based on images from surfaces densely covered with fluorophores, these variations are not significant over the length scale of the filaments. Finally, it is also possible that the filament is deformed either by adsorption to the surface or from compression by the AFM tip. To minimize this effect, care was taken to keep tip-sample forces as small as possible by adjusting the amplitude set point as close to the free amplitude as possible while still maintaining surface contact and image quality.

Consistent with past work on filaments formed under the pH 7 conditions used here, there appears to be an ''adventitious'' surface layer of myosin molecules that would explain the lack of a visible central bare zone (20,21). Nonphysiological conditions can sometimes enhance the bare zone (17), and for these filaments, molecular exchange of the innermost molecules with the surrounding medium is estimated to be negligible (22). The shell-like arrangement of myosin heads in ''pH 7 filaments'' sets some limits on the adventitious layer: the density of the total shell of heads, including both the adventitious layer and the core, is roughly constant for all filament heights and therefore along the filament length.

Myosin numbers from AFM and single-molecule TIRF imaging

Another test of the agreement of the two imaging methods is an estimate of the number of molecules in the filament based

TABLE 1 Myosins per filament as estimated from AFM height profiles and from TIRF intensity profiles after calibration of single-molecule fluorescence

Filament number	(Myosins/filament) by AFM	(Myosins/filament) by TIRF
i	436	316
ii	430	292
iii	59	70
iv	158	96
v	203	141

Filaments i–iii are shown in Fig. 2.

on each method. Because the structure of myosin is known, we can estimate the volume per molecule and compare it to the total filament volume. Each myosin molecule is modeled as a 150-nm-long rod with a 2-nm diameter and two heads that are each $10 \times 5 \times 3$ nm for a total volume per myosin of ~770 nm^3. Measuring volume from AFM images requires some knowledge of either the sample or tip shape. The tips we used in this case have a nominal initial radius of curvature at the tip between 10 and 40 nm; however, this can increase during scanning as a result of blunting against the surface or adsorption of material to the tip. The filament cross-sectional height profile shown in the inset in Fig. 2 *b* has a width at its base more than 10-fold greater than the height of 5 nm, implying that some broadening from the tip/sample convolution has indeed occurred or that the filament flattened somewhat during adsorption to the surface. In principle, the contributions of broadening and flattening could be assessed by performing a deconvolution using some assumption for the tip geometry, but because the filaments are only a few pixels across, this does not seem justified. Instead, we have chosen to assume that the filament has a circular cross section with a diameter equal to the filament height at that point and to calculate the volume based on this assumption. For this reason, our volume estimates from AFM should be taken as lower limits. Table 1 lists the results for five filaments that range from ~50 to 450 myosin motors per filament.

To estimate the number of molecules based on the TIRF data, we followed an analogous procedure and first determined the average intensity of single, well-separated myosin molecules. We imaged at high ionic strength (0.6 M KCl, 10 mM imidazole-HCl, 2 mM $MgCl_2$), ensuring that no filaments were formed, and then sought spots that bleached in one step, fitting them with a two-dimensional Gaussian (Appendix B). This procedure yields an average single-molecule intensity and was repeated each day immediately before filament experiments. The number of myosin motors per filament obtained from TIRF (Table 1) was thus obtained by comparing the average single-molecule intensity to the total intensity of a filament, and the estimates appear similar in magnitude to those obtained with AFM. Indeed, a plot of $N_{TIRF} = (\text{myosins/filament})_{TIRF}$ versus $N_{AFM} = (\text{myosins/filament})_{AFM}$ can be fit to a line: $N_{TIRF} = 11 + 0.67\,N_{AFM}$ ($R^2 = 0.98$). With TIRF, photobleaching of the fluorophores in the filament is unavoidable and could explain the persistent underestimate by ~33%. Depending on the arrangement of heads in the filaments, it is possible that fluorophore self-quenching could also contribute to this underestimate. The Förster radius for rhodamine self-quenching by resonant energy transfer is likely 4–5 nm (the Förster radius for homo-FRET of fluorescein, which has a similar overlap between its excitation and emission spectra, is 4.0 nm (23)). Based on the number of myosins per micrometer (see below), the average interhead distance is between 10 and 20 nm. Because of the rapid decay of the transfer efficiency with distance, the decrease in intensity from self-quenching should not be significant. In either case, a linear model provides an excellent fit in comparing AFM and TIRF.

Our determinations of motor numbers N_{TIRF} and N_{AFM} are in sufficiently good agreement with each other that we can estimate a mean motor density of ρ_{myo} of ~50–100 myosins/μm. This estimate for ρ_{myo} is ~25–50% of the physiological value in muscle of 210 molecules per micrometer (each crown of three molecules is separated by 14.3 nm (24)), and it is smaller still than an estimate based on the spacing of single fluorophores in sparsely labeled but otherwise similarly prepared filaments (25). In our experiments, a 30% decrease in filament heights from adsorption and/or compression under the tip would give a 50% underestimate for ρ_{myo}, and such dimensions ($\leq$2.5 nm decrease) are small and very possible when compared to myosin head and tail dimensions.

Filament asymmetry $\rho_{myo}(s)$

Because the fluorescent labels reside primarily in the myosin head, and the correlation of the data from our two modalities leads to a reasonable model of head arrangement as well as mutual agreement about ρ_{myo}, we can reasonably assume that the height variations seen along the filament contour s in AFM traces reflect the local density of myosin heads. The profiles for $\rho_{myo}(s)$ plotted in Fig. 2 *c* show that filaments are generally not symmetric about their midpoints. The fractional asymmetry δ is defined simply as the volume of one-half of the filament minus the volume of the other half divided by the total volume. The volumes are determined from the height profile as described above with the midpoint determined from the total filament length.

The results of this analysis are shown as inset numbers in Fig. 2 *c*, and the asymmetries measured from a larger set of filaments are summarized in Fig. 4, which includes data from filaments formed both by rapid mixing and by dialysis, with both showing similar values for the asymmetry. There is also no clear trend in the fractional asymmetry with length, highlighting the fact that even the shorter filaments formed by rapid mixing do not have physiological symmetry. The probability distribution $P(\delta)$ decreases almost linearly with increasing δ so that symmetric filaments are the most likely,

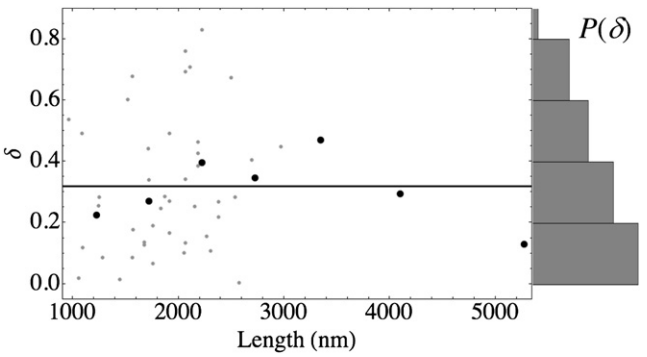

FIGURE 4 Fractional asymmetry from raw AFM height profiles as a function of length. Black points are averages over 500-nm bins of the individual data points shown in gray, except for the longest three points, which correspond to the three filaments imaged in Fig. 2. There is large scatter about the mean of 0.32 shown by the horizontal line, but there is no clear dependence on filament length. The right panel is a histogram showing the probability distribution of the filament asymmetries, δ. Small asymmetries are the most likely (the maximum of the distribution occurs at the smallest bin), but the decay with δ is slow (approximately linear).

but because the decay is not very rapid, the mean $\langle P(\delta)\rangle$ is still 0.32.

A purely entropic lattice model of asymmetric filaments

The lack of length dependence on the asymmetry as well as the decrease of $P(\delta)$ with δ can be captured using a purely entropic lattice model for the filaments. The brick-wall lattice with no overhangs shown in Fig. 5 *a* is motivated by the staggered packing of myosin molecules in filaments and has the desirable feature that filaments taper at their ends, as observed in experiments. If the binding energy is assumed to be constant for all sites, the statistical mechanical problem is reduced to a combinatorial problem: a purely entropic description of the equilibrium in this model thus depends only on the number of possible arrangements of molecules on the pyramidal lattice. Counting the number of ways of arranging bricks on this lattice is equivalent to counting the number of Dyck paths of the same size, i.e., the number of ways of connecting the two corners of a square region on a square lattice without crossing the line $y = x$. This is a useful equivalence to note (shown schematically in Fig. 5 *a*), because the solution of this second problem is known. The number of possible Dyck paths with base length L is given by the Catalan numbers (26):

$$C_L = \frac{(2L)!}{(L+1)!L!} \text{ for } L \geq 0.$$

To our knowledge, no analytical expression for the fractional asymmetry of these states is known, but it is possible to generate all possible Dyck paths for a given base length and to then calculate the fractional asymmetry δ for each of these model filaments.

Although C_L grows very rapidly with L, the results prove sufficiently informative for L up to 11, as shown in Fig. 5 b.

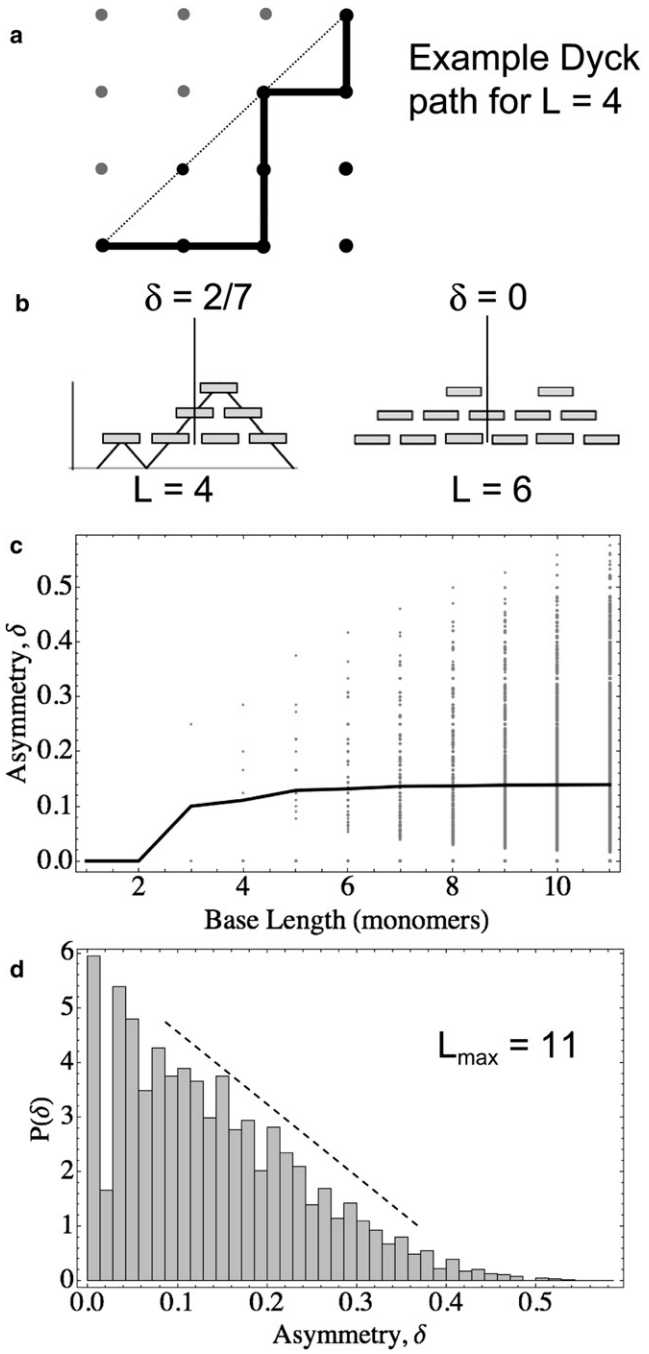

FIGURE 5 Pyramidal lattice model of myosin filaments. Myosin filaments are modeled using a lattice with staggered sites without allowing overhanging edges. The problem of counting the number of ways of stacking bricks on this lattice is equivalent to counting the number of ''Dyck paths'' (*a*). Two model filaments are shown in (*b*). To see the equivalence of these two problems, note that the path drawn behind the first filament is the same as that shown in *a* but rotated by $3\pi/4$. The base lengths L and fractional asymmetries δ are written in the insets. The height profiles of these filaments are equivalent to so-called Dyck paths as shown by the rotated plot under the first schematic filament. (*c*) Plot of δ as a function base length. Points show all possible model filaments of a given length. The line shows the average δ. (*d*) Histogram of the points plotted in (*b*) showing dependence of $P(\delta)$ on δ.

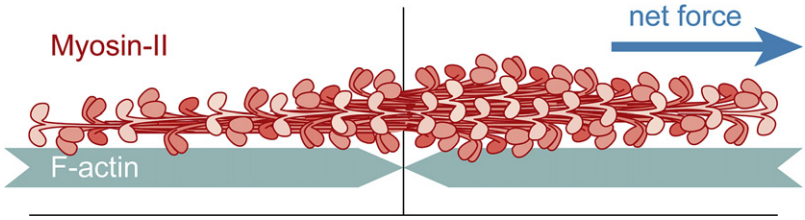

FIGURE 6 Asymmetric myosin filaments could be motile as shown in this schematic of an asymmetric myosin filament at an F-actin junction. If the myosin filament (*top*) is bipolar about its center, and the actin filaments (*bottom*, minus ends toward center) are relatively immobile, then the contractile forces exerted by the myosin filament on the actin filaments will not balance. If there is sufficient asymmetry, the myosin filament will move toward the side with more heads (in this case to the right).

δ is zero for filaments of length $L = 1$ and 2, but this rises and rapidly plateaus, reaching a nearly constant value. Thus, the pyramidal lattice model qualitatively captures the length dependence of δ shown in Fig. 4. The asymptotic value of 0.14 is about half the experimental value, but it is important to note that these planar model filaments with a base length of 11 can have up to 66 molecules in them so that the size ranges explored in the model are comparable to the shorter filaments observed in AFM.

The form of $P(\delta)$ predicted by the model (Fig. 5 *c*) is also qualitatively similar to the experimental distribution: small δ is the most likely, but most of the filaments are asymmetric. One difference between the distribution predicted by the model and that observed in AFM is the range of the data. The maximum asymmetry predicted for filaments of length $L = 11$ is 0.5, whereas experimental values occasionally reach above 0.7. This is partly because of the limited length L that is accessible because, as is clear from the plot in Fig. 5 *b*, the upper range of asymmetries is still increasing even if the average is not. Nonetheless, given the simplicity of the pyramidal lattice model considered here, the qualitative agreement suggests that even a slightly more sophisticated model of synthetic filaments might capture more details of the filament structure and perhaps also give insight into the kinds of regulatory mechanisms that control filament symmetry in vivo.

Asymmetry implies a force imbalance

Because these asymmetries are correlated with the number of heads on either half of the filament, asymmetric filaments imply a force imbalance even if the filaments are bipolar and are attached to oppositely oriented actin filaments, as shown schematically in Fig. 6. In other words, in a cross-linked network of actin filaments, as used in active gel experiments (8), where the actin network is relatively immobile, myosin filaments might not be simply contractile but in fact motile, because even at a junction, asymmetric filaments should move toward the end with more heads. Furthermore, on a single filament or bundle of parallel actin filaments with the same polarity, even symmetric filaments are expected to be motile given the results of actin-gliding assays that show that actin can travel in both directions along both parts of myosin filaments, albeit more slowly in the nonphysiological direction (6,7). This kind of motility could be important for the comparison between models of active gels and quantitative data on contractility (27). In future experiments, the potential motility of myosin in active gels could be determined in a straightforward way by using different color labels for myosin and actin.

In muscle, filament length and symmetry are tightly controlled, but less is known about the structure of stress fibers in nonmuscle cells. Although several proteins are involved, their role in controlling myosin filament symmetry is unknown, and slight asymmetries in myosin minifilaments could be particularly important in nonmuscle cells. It has already been proposed that myosin filaments could be motile—rather than purely contractile—in stress fibers with uniform polarity (28), but this may even be the case in sarcomere-like stress fibers if there is a force imbalance caused by asymmetric myosin filaments. This kind of motility could serve simply to transport myosin or could perhaps be involved in cargo transport as other myosins are known to be (29). In any case, if filament motility is absent in nonmuscle cells, this may imply that there is a mechanism regulating nonmuscle myosin filament symmetry or some other mechanism to stabilize asymmetric filaments in actin bundles or junctions.

CONCLUSIONS

Cross-correlated TIRF/AFM provides complementary advantages for sample characterization: TIRF can leverage the extensive chromophore and fluorescent protein technology that has been developed to specifically identify molecular species of interest, whereas AFM can be used to collect high-resolution structural information from the same sample region. Furthermore, a quantitative correlation of the data from the two modalities provides structural information that would have been unavailable from either one alone. In particular, we were able to confirm that the heads of myosin filaments are arranged in a shell of roughly constant thickness around the filament, consistent with having the heads exposed to the outside as required for their actin-binding function. It also shows the power of correlative TIRF/AFM to determine the arrangement of fluorophores within a structure that is only nanometers thick in fluid at room temperature. The same method can be extended to other macromolecular structures that can be fluorescently labeled and deposited on a surface.

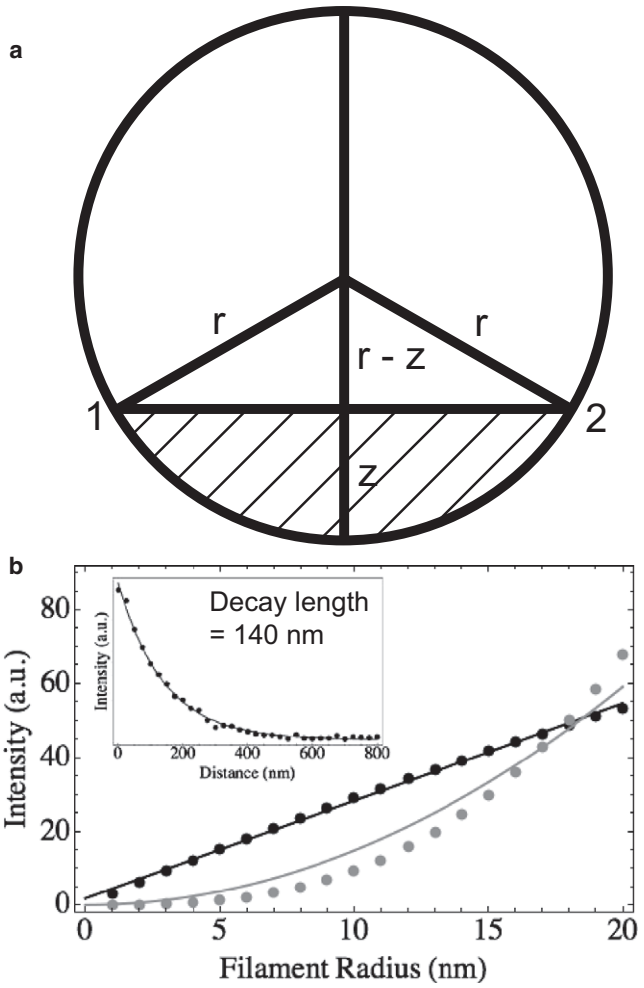

FIGURE 7 (*a*) Geometry for scaling correction calculation. The region with fluorophores for the shell model is the arc of the circle between the points labeled 1 and 2. The region with fluorophores for the solid model is the segment indicated by the thin lines. (*b*) The results of the numerical integration for the shell model (*black points*) and solid model (*gray points*) taking into account the decay of the TIRF field. The solid lines are fits to the data—linear in the case of the shell model and quadratic (no constant or linear term) in the case of the solid model.

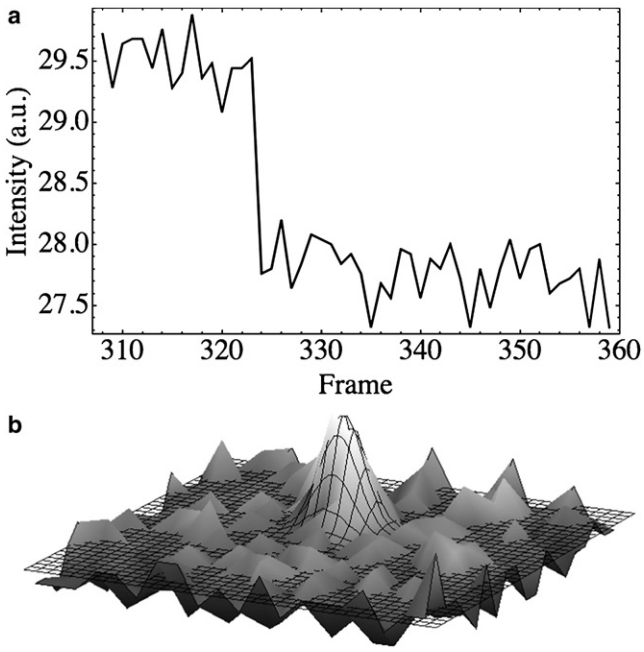

FIGURE 8 (*a*) Average intensity over time for a 5 by 5 pixel square showing a one-step bleaching event. (*b*) A Gaussian fit to a spot that subsequently bleached in a single step to determine that spot's total intensity.

Using the structural information revealed by AFM images of myosin filaments, we quantified the fractional asymmetry of synthetic filaments and found that it averaged 0.32 for filaments prepared by rapid mixing and by dialysis and over the length range we observed. This asymmetry could have implications for intracellular trafficking (28), in vitro motility measurements (7), and for experiments using myosin to activate actin gel systems (27).

APPENDIX A: TIRF EXCITATION SCALING CORRECTION

The electric field intensity in TIRF decays exponentially from the sample surface. The corresponding decay of the fluorescence intensity from a dye near the surface is more complicated because of interaction with the surface, as discussed in detail by Hellen and Axelrod (30). However, although these corrections can be important for comparing the intensity of a fluorophore near a surface with one far away from the surface, the corrections vary slowly with height within the first 10 nm, which is the relevant scale for our measurements. This was confirmed by measuring the drop in intensity from fluorophores on the tip of an AFM cantilever as it was moved away from the sample surface (Fig. 7 *b*, *inset*). The intensity is fit well by a single exponential with a decay length of 140 nm. This exponential decay in fluorescence intensity introduces a deviation from linear intensity scaling even for a filament that is a perfect cylinder with fluorophores arranged only around its circumference. However, for reasonable assumptions for the filament properties in our experiments, this correction is negligible for the case of fluorophores distributed in a shell. To see this, consider the geometry shown in Fig. 7 *a*. It depicts a filament cross section of radius r sitting on a surface at $z = 0$, where z is the height above the surface. The fluorescence intensity from this cross section is then proportional to the integrated contributions of the fluorophores around the edge times the excitation intensity at each height:

$$I_{fl}\alpha\int_0^{2r}\exp[-z/d]l_{arc}dz$$
$$\alpha\int_0^{2r}\exp[-z/d]\left(2r\cos^{-1}\left[\tfrac{r-z}{r}\right]\right)dz,$$

where l_{arc} is the length of the arc between points 1 and 2 in Fig. 7, I_{fl} is the fluorescence intensity, and d is the characteristic decay length of the evanescent field. Using a decay length of 150 nm, the above expression for I_{fl} was integrated numerically in Mathematica (Wolfram Research, Champagne, IL) for several values of filament radius up to 20 nm. As shown by the linear fit in Fig. 7 b, the correction for the decay of the evanescent field is negligible compared to the experimental scatter in Fig. 3 a. A similar procedure can be carried out for the case when the fluorophores are assumed to fill the cylinder uniformly. In this case, rather than the arc length appearing above, we have the area of a segment of the circular cross-section given by

$$A_{seg} = \frac{r^2}{2}\left(2\cos^{-1}\left[\frac{r-z}{r}\right] - \sin\left[2\cos^{-1}\left[\frac{r-z}{r}\right]\right]\right).$$

The scaling resulting from this correction is still distinguishable from a linear scaling, although it is no longer perfectly quadratic (Fig. 7 *b*).

APPENDIX B: SINGLE-MOLECULE INTENSITY CALIBRATION

To determine the single fluorophore intensity, we used a sample of mostly singly labeled myosin monomers and found spots that bleached in one step by monitoring the intensity over time in a square region of five pixels on a side (Fig. 8 a). We then fit a two-dimensional Gaussian to the spot before its bleaching and used the volume of the best-fit Gaussian as the spot's total intensity (Fig. 8 *b*).

This work was funded by National Science Foundation grant NSEC DMR04-25780 to the Nano/Bio Interface Center and CMS05 56259 to D.E.D., and also National Institutes of Health grants (D.E.D.). A.E.X.B. is partially supported by a scholarship from the Natural Sciences and Engineering Research Council of Canada. We also thank Andrea Rehfeldt (http://www.az-design.de/) for the schematic in Fig. 6, John Beausang for help with single-molecule measurements, and Klara Stefflova, Florian Rehfeldt, and Irena Ivanovska for critical reading of the manuscript.

REFERENCES

1. Conti, M. A., and R. S. Adelstein. 2008. Nonmuscle myosin II moves in new directions. *J. Cell Sci.* 121:11–18.
2. Ip, K., A. Sobieszek, D. Solomon, Y. Jiao, P. D. Par, et al. 2007. Physical integrity of smooth muscle myosin filaments is enhanced by phosphorylation of the regulatory myosin light chain. *Cell. Physiol. Biochem.* 20:649–658.
3. Decker, B., and M. S. Z. Kellermayer. 2008. Periodically arranged interactions within the myosin filament backbone revealed by mechanical unzipping. *J. Mol. Biol.* 377:307–310.
4. Davis, J. S. 1988. Assembly processes in vertebrate skeletal thick filament formation. *Annu. Rev. Biophys. Biophys. Chem.* 17:217–239.
5. Sellers, J. R., and B. Kachar. 1990. Polarity and velocity of sliding filaments—control of direction by actin and of speed by myosin. *Science.* 249:406–408.
6. Yamada, A., and T. Wakabayashi. 1993. Movement of actin away from the center of reconstituted rabbit myosin filament in slower than in the opposite direction. *Biophys. J.* 64:565–569.
7. Scholz, T., and B. Brenner. 2003. Actin sliding on reconstituted myosin filaments containing only one myosin heavy chain isoform. *J. Muscle Res. Cell Motil.* 24:77–86.
8. Mizuno, D., C. Tardin, C. F. Schmidt, and F. C. MacKintosh. 2007. Nonequilibrium mechanics of active cytoskeletal networks. *Science.* 315:370–373.
9. Huxley, H. E. 1963. Electron microscope studies on structure of natural and synthetic protein filaments from striated muscle. *J. Mol. Biol.* 7:281–308.
10. Chowrashi, P. K., and F. A. Pepe. 1986. The myosin filament 12. Effect of MgATP on assembly. *J. Muscle Res. Cell Motil.* 7:413–420.
11. Barral, J. M., and H. F. Epstein. 1999. Protein machines and self assembly in muscle organization. *Bioessays.* 21:813–823.
12. Margossian, S. S., and S. Lowey. 1982. Preparation of myosin and its subfragments from rabbit skeletal-muscle. *Methods Enzymol.* 85:55–71.
13. Sutoh, K. 1981. Location of SH1, and SH2 along a heavy chain of myosin subfragment. 1. *Biochemistry.* 20:3281–3285.
14. Kocsis, E., B. L. Trus, C. J. Steer, M. E. Bisher, and A. C. Steven. 1991. Image averaging of flexible fibrous macromolecules—the clathrin triskelion has an elastic proximal segment. *J. Struct. Biol.* 107: 6–14.
15. Toprak, E., and P. R. Selvin. 2007. New fluorescent tools for watching nanometer-scale conformational changes of single molecules. *Annu. Rev. Biophys. Biomol. Struct.* 36:349–369.
16. Hell, S. W. 2007. Far-field optical nanoscopy. *Science.* 316:1153–1158.
17. Kaminer, B., and A. L. Bell. 1966. Myosin filamentogenesis—effects of pH and ionic concentration. *J. Mol. Biol.* 20:391–394.
18. Akaike, H. 1974. A new look at the statistical model identification. *IEEE Trans. Automat. Contr.* 19:716–723.
19. Motulsky, H. A. C. 2004. Fitting Models to Biological Data Using Linear and Nonlinear Regression: A Practical Guide to Curve Fitting. Oxford University Press, New York.
20. Saad, A. D., J. D. Pardee, and D. A. Fischman. 1986. Dynamic exchange of myosin molecules between thick filaments. *Proc. Natl. Acad. Sci. USA.* 83:9483–9487.
21. Saad, A. D., J. E. Dennis, I. P. Tan, and D. A. Fischman. 1991. Visualization of myosin exchange between synthetic thick filaments. *J. Muscle Res. Cell Motil.* 12:225–234.
22. Davis, J. S. 1993. Myosin thick filaments and subunit exchange—a stochastic simulation based on the kinetics of assembly. *Biochemistry.* 32:4035–4042.
23. Chen, Y., D. E. Anderson, M. Rajagopalan, and H. P. Erickson. 2007. Assembly dynamics of *Mycobacterium tuberculosis* FtsZ. *J. Biol. Chem.* 282:27736–27743.
24. Stewart, M., and R. W. Kensler. 1986. Arrangement of myosin heads in relaxed thick filaments from frog skeletal muscle. *J. Mol. Biol.* 192:831–851.
25. Conibear, P. B., and C. R. Bagshaw. 2000. Myosin monomer density and exchange in synthetic thick filaments investigated using fluorescence microscopy with single molecule sensitivity. *Proc. R. Soc. Lond. B. Biol. Sci.* 267:415–421.
26. Lothaire, M. 2005. Applied combinatorics on words. *In* Encyclopedia of Mathematics and its Applications. P. Flajolet, M. Ismail, and E. Lutwak, editors. Cambridge University Press, Cambridge.
27. Bendix, P. M., G. H. Koenderink, D. Cuvelier, Z. Dogic, B. N. Koeleman, et al. 2008. A quantitative analysis of contractility in active cytoskeletal protein networks. *Biophys. J.* 94:3126–3136.
28. Pellegrin, S., and H. Mellor. 2007. Actin stress fibres. *J. Cell Sci.* 120:3491–3499.
29. Ana, S., and G. M. L. DePina. 1999. Vesicle transport: The role of actin filaments and myosin motors. *Microsc. Res. Tech.* 47:93–106.
30. Hellen, E. H., and D. Axelrod. 1987. Fluorescence emission at dielectric and metal-film interfaces. *J. Opt. Soc. Am. B.* 4:337–350.